Helmholtz-Zentrum Dresden-Rossendorf (HZDR)

HZDR
HELMHOLTZ ZENTRUM
DRESDEN ROSSENDORF

Defects distribution and evolution in selected-area helium ion implanted 4H-SiC

Song, Y.; Xu, Z.; Rommel, M.; Astakhov, G.; Hlawacek, G.; Fang, F.;

Originally published:

December 2023

Ceramics International 50(2024)5, 7691-7701

DOI: https://doi.org/10.1016/j.ceramint.2023.12.096

Perma-Link to Publication Repository of HZDR:

https://www.hzdr.de/publications/Publ-37512

Release of the secondary publication
on the basis of the German Copyright Law § 38 Section 4.

Defects distribution and evolution in selected-area helium ion implanted 4H-SiC

Ying Song [a,*], Zongwei Xu[a,*], Mathias Rommel[b], Georgy V. Astakhov[c], Gregor Hlawacek[c], Fengzhou Fang[a,d]

[a] State Key Laboratory of Precision Measuring Technology and Instruments, Centre of Micro/Nano Manufacturing Technology, Tianjin University, Tianjin 300072, China

[b] Fraunhofer Institute for Integrated Systems and Device Technology (IISB), Schottkystrasse 10, 91058 Erlangen, Germany

[c] Institute of Ion Beam Physics and Materials Research, Helmholtz-Zentrum Dresden-Rossendorf (HZDR), Bautzner Landstrasse 400, 01328 Dresden, Germany

[d] Laboratory of Micro/Nano Manufacturing Technology (MNMT-Dublin), University College Dublin, Ireland

*Authors to whom correspondence should be addressed: songying@tju.edu.cn, zongweixu@tju.edu.cn

Abstract

Color centers in silicon carbide has been widely studied in view of the promising near-infrared emission near the low-loss telecom wavelengths as well as the maturity of semiconductor technology of silicon carbide material. Recently, there is an urgent need to generate color centers in predetermined location so as to integrate with photonic cavities of waveguides. In this paper, we report an experimentally demonstration of the generation of V_{Si}, $C_{Si}V_C$, and N_CV_{Si} color centers in 4H-SiC using helium ion microscope in 5×5 μm areas with subsequent annealing treatment. Combined with transmission electron microscopy (TEM), photoluminescence (PL) and cathodoluminescence (CL) spectroscopy and Raman stress analysis, the evolution and distribution of color centers were thoroughly investigated. Cross-sectional TEM revealed the presence of helium bubbles in center of the implanted region with high doses which account for the observed quench of PL emission in center of the implanted regions in both PL and CL measurements. PL spectra from the virgin, implanted and annealed

samples proved the appearance of V_{Si} after implantation and the transformation from V_{Si} to $C_{Si}V_C$ and N_CV_{Si} centers after annealing at 1000 °C. Moreover, as the increase of the implantation dose, the area of N_CV_{Si} centers increases whereas that of $C_{Si}V_C$ decreases, which implied a competitive relationship between the formation of $C_{Si}V_C$ and N_CV_{Si} defects. The comparison between stress distribution and $C_{Si}V_C$ defect distribution illustrated that $C_{Si}V_C$ centers predominantly distributed around the surface rupture region after thermal annealing where significant stress repair occurred. The results suggest that focused helium ion implantation holds promise for the precise coupling of V_{Si}, $C_{Si}V_C$ and N_CV_{Si} centers in predefined location in integrated photonics applications.

Keywords

Silicon carbide; color center; defects; ion implantation; photoluminescence; Raman; Stress; cathodoluminescence

1. Introduction

Silicon carbide (SiC) has been serving as starting material for decades in power electronic devices used in high-voltage and high-temperature environment. In recent years, studies on the application of SiC as host material for quantum devices has increased remarkably, in which various fluorescent point defects, also called color centers, play a key role in quantum technologies such as single photon source [1-3], spin-qubit carriers [4-7] and quantum sensors with respect to electrical filed [8], magnetic field [9, 11, 12], strain [13], and temperature sensing [14, 15]. More than 200 polytypes of SiC have been reported which have different stacking sequence of atomic layers, and the most relevant polytypes are 3C-(cubic), 4H-(hexagonal), and 6H-SiC(hexagonal). Among them, 4H-SiC is the most extensively studied polytype owning to its maturity in large-scale growth and superiority in control of growth defect. Therefore, in this study, commercially available nitrogen-doped 4H-SiC was used as the platform for color center fabrication.

In terms of color centers in 4H-SiC, numerous investigations have focused on four types of point defects, including the silicon monovacancy (V_{Si}) [2], the carbon antisite-vacancy pair ($C_{Si}V_C$) [1], the neutral divacancy ($V_{Si}V_C$) [16] and silicon vacancy-nitrogen pairs (N_CV_{Si}) [17]. The emission of those four types of color centers covers bands from visible to near-infrared

(NIR) wavelengths. And color centers emitting in NIR band are especially favorable in biological analyses [18, 19]. As a typical parameter describing luminous properties, zero-phonon line (ZPL) usually emerge at cryogenic temperature, which determine the line shape of PL emission together with phonon sideband. Color centers in 4H-SiC can usually be observed with more than one ZPL due to the presence of two inequivalent lattice sites in the unite cell. The two inequivalent sites are usually termed as hexagonal (denoted *h* site) and cubic (denoted *k* site), depending on whether the configuration of the nearest-neighbors is similar to that of the hexagonal würtzite or that of the cubic zinc blende structure. The ZPLs of above-mentioned four types of color centers, which have been verified in experiments are listed in Table 1.

Table.1 ZPLs of typical color centers in 4H-SiC.

Type	$C_{Si}V_C$ [1]		V_{Si} [20]		$V_{Si}V_C$ [16]		N_CV_{Si} [17]	
ZPLs	A1	648.5 nm	V1	861.3 nm (h)	PL1	1137.6 nm (kk)	PLX1	1242.5 nm (kk)
	B2	672.8nm	V2	916.1 nm (k)	PL2	1127.3 nm (hh)	PLX2	1241.2 nm (hh)
	B3	675.0 nm			PL3	1107.1 nm (hk)	PLX3	1222.9 nm (hk)
	B4	676.3 nm			PL4	1078.3 nm (kh)	PLX4	1179.8 nm (kh)

Color centers can be intentionally introduced in silicon carbide using energetic particle irradiation technologies like ion implantation [5, 21-26] and direct laser writing [27]. However, the generation of color centers in predetermined location is still an urgent need in the integration with photonic cavities and waveguides [28, 29] for quantum applications. Here, we focus on the formation of V_{Si} in 4H-SiC by helium ion implantation using helium ion microscope (HIM) and observed its transformation into $C_{Si}V_C$ and N_CV_{Si} centers after subsequent annealing treatment. Further, we report the distribution of V_{Si}, $C_{Si}V_C$ and N_CV_{Si} centers collected by PL and CL measurement and discuss the distribution of different doses in combination with TEM and Raman stress measurements. Finally, a competitive relationship between the yield of $C_{Si}V_C$ and N_CV_{Si} centers is demonstrated.

2. Material and methods

2.1 Materials and sample treatments

The starting material was commercial single crystalline nitrogen-doped (0001) 4H-SiC with 4°± 0.5° off-axis from *Xiamen Powerway Advanced material Co., Ltd.* (PAM-XIAMEN). Selective helium ion implantation was achieved by helium ion microscope (ORION NanoFeb, Zeiss) with energy of 30 kV at around 300 K. Implanted regions are 5 μm apart and in square shape of 5 μm × 5 μm with wide doses ranging from 1.0×10^{14} cm^{-2} to 1.0×10^{18} cm^{-2}. Next, implanted silicon carbide was annealed in a N_2 atmosphere at 1000 °C for one hour to stimulate the migration and recombination of point defects.

2.2 Transmission electronic microscope

After implantation, three cross sections with implantation doses of 3.5×10^{15} cm^{-2}, 5.6×10^{16} cm^{-2} and 5.0×10^{17} cm^{-2} were prepared by focused ion beam (FIB) to allow morphology observation by transmission electronic microscope (TEM). Cross sections prepared by FIB (Helios 5, Thermo-Fisher Scientific) with a thickness of about 100 nm were observed by TEM (Tecnai G2 F20, FEI) at 200 kV. The observation was made using bright field mode and selected region electron diffraction (SAED) mode.

2.3 Simulation

Monte Carlo simulation were carried out to estimate the radiation damage and He distribution using the stopping and range of ions in matter (SRIM-2013) [30]. Full damage cascades calculation mode was adopted to guarantee the accuracy of calculation. An average displacement threshold energy of 35 eV for Si atom and 21 eV for C atom were chosen as suggested by [31] and [32]. The density of silicon carbide was set as 3.21 g/cm^3.

2.4 Spectral measurement

Photoluminescence (PL) was measured to identify the defect configuration. Residual stress was formulated by Raman measurement with real-time calibration. In this study, all confocal PL and Raman spectra were performed using a custom-built spectral system equipped with a spectrometer iHR550 (Horiba), a silicon-based charged-coupled device camera (CCD, Synapse, Horiba) used in the wavelength range from 200 to 1050 nm, and an InGaAs detector (2 mm diameter indium gallium arsenide photodiode, DSS-IGA020T, Horiba) used in the wavelength range from 800 to 1050 nm. Backscattering configuration was used in PL and

Raman measurement. Four different wavelengths, including 405 nm, 532 nm, 785 nm, and 1064 nm, were used as the source of excitation in spectral measurement. The excitation laser was focused on sample using a ×100 objective (NA=0.9, Olympus).

Spectral mapping was realized by placing the sample on a *xy*-piezoelectric scanner with repeated positioning accuracy of 50 nm. Before the spectral acquisition, the samples are mounted firmly on a slide by conductive adhesive. Then they are placed still for half an hour for stabilization to avoid the influence of the sample drift caused by the environmental disturbance. Low temperature PL spectra were measured using compatible temperature control stage THMS600 (Linkam Scientific, UK). Sample were frozen from room temperature 297 K down to 77 K by liquid nitrogen with accuracy and stability of 0.01℃.

2.5 Cathodoluminescence

Cathodoluminescence (CL) system (*Golenscope Tech*, China) were employed in an attempt to enable nanoscale spatial resolution. The system is equipped with iHR320 spectrometer (Horiba, Japan) and an electrical cooled charged-coupled device camera (Synapse, Horiba). The excitation voltage of electron beam was 5 kV accompanied with beam current of 70 μA and grating of 150 gr/mm in cathodoluminescence spectra measurement.

3. Results and discussion

3.1 Morphology

In order to introduce color centers in specific location in SiC, helium ion microscope was used to implant He^+ in square areas of 5μm×5μm with doses ranging from 1.0×10^{14} cm^{-2} to 1.0×10^{18} cm^{-2}. Fig. 1 displays the cross-sectional TEM (XTEM) of three orders of helium implantation doses: 3.0×10^{15} cm^{-2}, 5.6×10^{16} cm^{-2} and 5.0×10^{17} cm^{-2}. The corresponding peak damage doses were calculated as 0.14, 2.64, and 23.59 displacement per atom (dpa) [33] by SRIM-2013 software.

The maximum He^+ concentration was simulated to be 210 nm under the sample surface, and the maximum vacancy concentration was predicted to be shallower at 160 nm under the sample surface, as evident from the overlapped depth profiles in Fig. 1(a). The insert in Fig. 1(a) shows the SAED pattern at the depth of the damage peak, confirming that the material remains crystalline after He^+ implantation with a dose of 3.0×10^{15} cm^{-2}. When implanting with

a higher dose of 5.6×10^{16} cm^{-2}, as shown in Fig. 1(b), amorphous is observed in the implanted region, accompanied by the swelling of the sample surface of around 40 nm compared to the un-implanted surface. And the lateral damage range of the amorphous cocoon shape at the edge of the implanted area was clearly visible of around 50 nm, which is smaller than the predicted lateral straggling range of vacancies of around 240 nm by SRIM simulation. This difference is due to the lateral damage far from the implantation boundary is mainly isolated point defects, which have not accumulated and reached the amorphous state that enough to show in TEM contrast, but will be counted as the lateral straggling range of vacancies by SRIM. SAED patterns, labeled as *A*, *B*, and *C*, were obtained near the boundary of the implantation region, which can be seen in the right of Fig.1(b). The clear diffraction spots in zone *A* reveals the intact crystal structure. By contrast, the halo patterns of zone *C* verify the amorphous feature in implanted region. However, the SEAD pattern in zone *B* presents a both concentric circles and diffraction spots, indicating that the material at the borderline with black contrast is partially amorphous, but still retains some lattice structure. Apart from the amorphous character induced by implantation, a cloud of small bubbles as indicated by red circles in Fig.1(c) is also observed at around 210 nm below the sample surface, which correlates well with the aforementioned location of maximum He^+ concentration by SRIM.

For the sample irradiated with 5.0×10^{17} cm^{-2} of He^+, swelling became manifest and was estimated to around 160 nm in the center of implanted region from Fig. 1(d), which is in line with the precious results discovered by atomic force microscope (AFM) in [34]. Obvious lateral damage was observed at the edge of the implanted area, and white contrast helium bubble clusters appeared in the center of the implanted region. SAED patterns in Fig. 1(e) shows that crystalline has been appreciably destroyed and became amorphous in implanted region *C*, whereas the clear lattice diffraction pattern proves good lattice integrity in both region *A* and *B*. Also, as shown in Figs. 1(e) and (f), a lot more and larger bubbles arise in the implanted region compared to those of 5.6×10^{16} cm^{-2}, which presents a layered arrangement in a sandwich structure according to the size of bubbles. The sandwich-structured bubble band is estimated to be 170~330 nm below the swelled surface. Large bubble with size range of 75 to 95 nm is sandwiched between two other layers with smaller bubbles size no more than 25 nm. As for the spread range of bubbles, the helium bubble on the side near the surface is more widely distributed when using the center of the large helium bubble as a benchmark, possibly because helium diffuses more easily toward the surface than into deep of the sample.

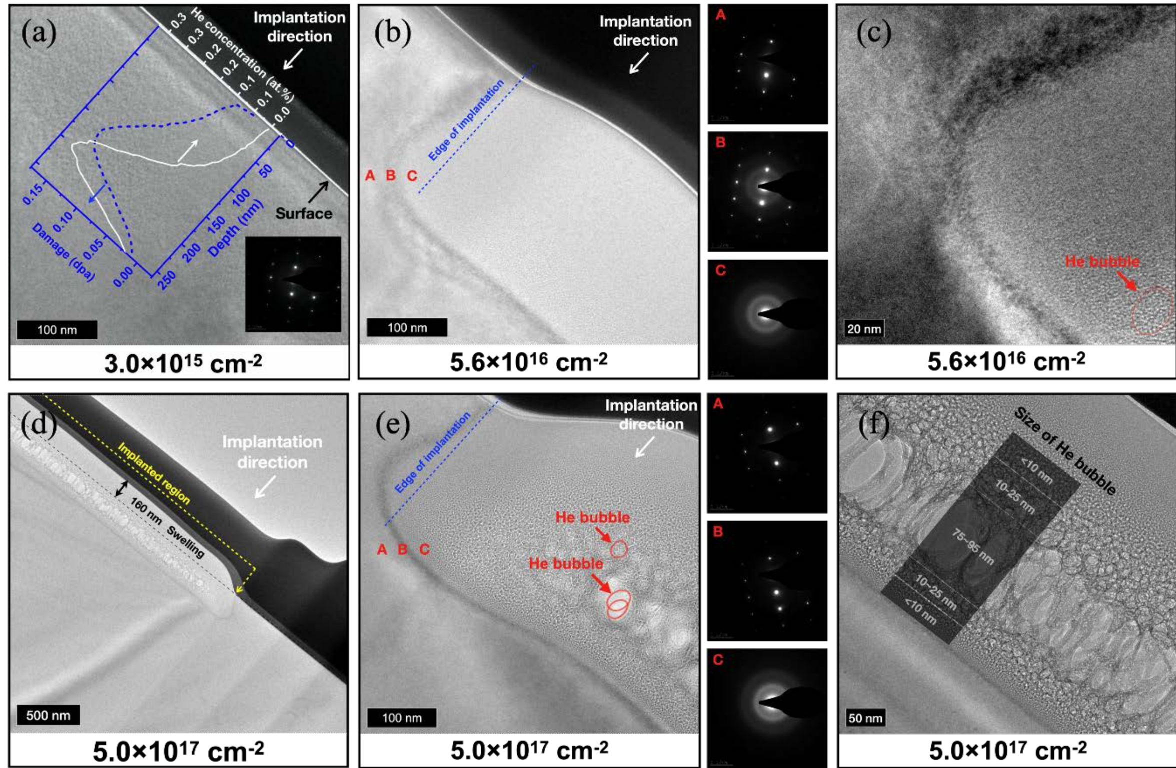

Fig. 1. TEM morphology of He^+ implanted regions with dose of (a)3.0×10^{15} cm^{-2}; (b) and (c) 5.6×10^{16} cm^{-2} and (d-f) 5.0×10^{17} cm^{-2}. The overlapped plots in Fig. 1(a) are He and vacancy depth profiles given by SRIM calculation, using implantation energy of 30 keV, average displacement threshold energy of 35 eV for Si atom and 21 eV for C atom, respectively. SAED pattern in Fig. 1(a) is from the depth of around 150 nm which is close to the predicted maximum vacancy concentration depth. Insert SAED patterns in Figs. 1(b) and (e) are from the place near the ion implantation boundary and are labeled as A, B and C for outside of the implantation region, on the boundary, and inside of the implantation region.

The threshold dose for the formation of observable helium bubbles has been found about 0.18 dpa in the peak damage for room temperature He^+ implantation [35]. Thus, it can be deduced that the threshold dose of the formation of helium bubble for 30 keV He^+ implantation was around 4.0×10^{15} cm^{-2} [36] which corresponds to 0.18 dpa. This value is in good agreement with the observations in our experiments. That is, no helium bubbles appear in low doses (3.0×10^{15} cm^{-2}, 0.14 dpa), while obvious helium bubbles appear in moderate (5.6×10^{16} cm^{-2}, 2.64 dpa) and high doses (5.0×10^{17} cm^{-2}, 23.59 dpa).

3.2 Cathodoluminescence

Previous studies [34, 37] have demonstrated the distribution of PL in He^+ implanted V_{Si}, which shows an intensity pattern of weak center and strong edge of the implanted area with implantation dose larger than 1.0×10^{16} cm^{-2}. The reduction of the PL in the center of implanted region has been attributed to the appearance of amorphous as well as the He bubbles, when the dose exceeds 1.0×10^{16} cm^{-2}. Here, in order to improve the lateral resolution of the distribution of V_{Si}, we performed cathodoluminescence (CL) spectroscopy measurement at room temperature for the region with the He^+ implantation dose above 5.0×10^{15} cm^{-2}, as shown in Fig. 2. The CL spectra were measured with a scanning electron microprobe (SEM) equipped with a converging mirror for signal collection, an optical fiber for signal transmission, a spectrometer iHR320 (Horiba) with focal length of 300 mm, and a thermoelectrically-cooled CCD (Synapse, Horiba).

First, we measured CL spectrum in virgin and implanted position with a dose of 5.0×10^{15} cm^{-2}, as given in Fig. 2(a). The spectra from virgin area shows a broad peak centered at 580 nm, which is identified as the screw dislocation in accordance with [38]. As for the CL spectra from implanted region, apart from the 580 nm peak, a lower PL peak located at 900 nm appears, corresponding to the emission from V_{Si} defects [39]. Then, we performed a set of line scan measurements across the implanted square area to determine the lateral distribution range of V_{Si} defects. Fig. 2(b) displays the secondary electron scanning imaging image of the implanted region with a dose of 5.6×10^{16} cm^{-2}, along with a line across the implanted area showing the scanned path with 9.78 μm in length and 155.3 nm in step (64 points in total for each line scan). As illustrated in Fig. 2(c), each spectrum at wavelengths from 478.7 nm to 1015.8 nm was represented as a normalized color bar in which red color is strong in CL intensity and blue means weak CL intensity. Color bars from 64 points in each scanned line were arranged according to the measurement position. The horizontal black blocks at the top of the color maps indicated the implanted range in the line scan. As expected, two emissions from screw dislocation of the substrate (580 nm) and V_{Si} (900 nm) defects are observed, the latter of which are concentrated in the edge of implantation with lateral spread distance of around 2 μm. In addition, as the increase of implantation dose, the screw dislocation signal from substrate decreases whereas the emission from silicon vacancy increases near the implantation edge, corresponding well with the variation of V_{Si} distribution by PL measurement at different doses [34, 37]. The decrease of both emission at 580 nm and 900 nm in the center of implanted region

imply that the fluorescence quenching occurred due to the formation of amorphous and helium bubbles, which is consistent with the results of PL and TEM.

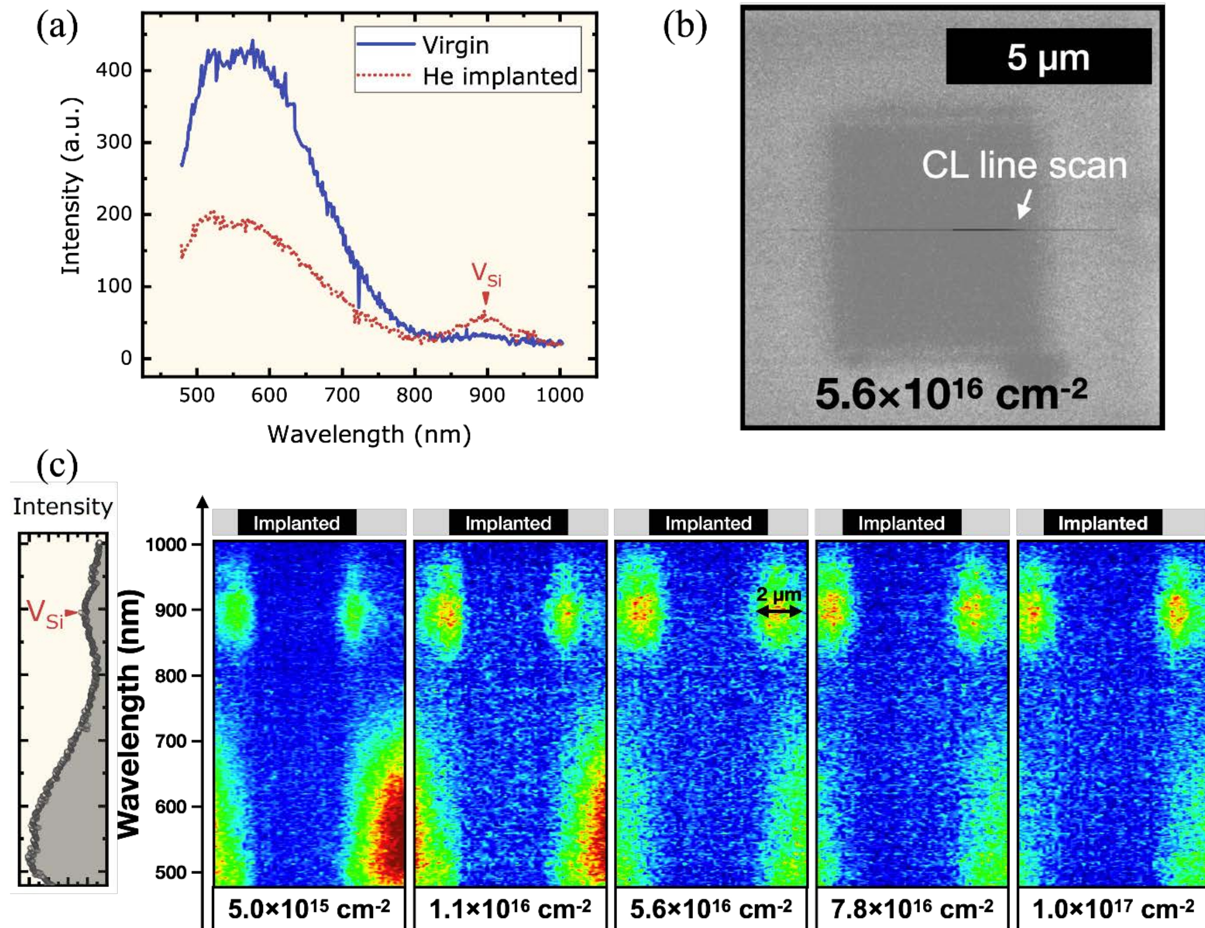

Fig. 2. (a) Cathodoluminescence of the virgin and implanted region measured at 300 K using excitation voltage of 5 kV, beam current of 70 μA and grating of 150 gr/mm. (b) The secondary electron scanning imaging of the He^+ implanted region with a dose of 5.6×10^{16} cm^{-2}. The grayscale line across the implanted square area is the position of the CL line scan, of which the step size is 155 nm. (c) The normalized line scan results were plotted according to the location of measurement in CL line scan, with wide dose range from the order of 10^{15} cm^{-2} to 10^{17} cm^{-2}, where red color represents stronger intensity.

3.3 Transformation of point defects after annealing treatment

In order to generate the promising color centers in SiC at NIR biological transparency window [40], annealing treatment is required to activate the migration and recombination of point defects. 4H-SiC samples implanted by He^+ ions were annealed in N_2 atmosphere at 1000 °C for 1 hour. We measured PL spectrum of the samples in three stages: before implantation (labeled as virgin); after implantation without annealing; after implantation with subsequent annealing treatment, using different excitation wavelengths of 532 nm, 785 nm and 1064 nm, as displayed in Fig. 3.

For virgin sample, there is no PL signals from wavelength range of 500 to 1600 nm, proving that the original 4H-SiC is pure and free of color centers, as shown in Figs. 3(a)(d) and (g). Compared with PL spectrum of the virgin sample, a broad PL peak centered at 900 nm appeared in the implanted sample using excitation of 785 nm from Fig. 3(e), which has been identified as V_{Si} defect by the ZPLs (V1 at 859 nm and V2 at 916 nm) in PL spectrum at 77 K as shown in Fig. 4(a) and in our previous study [34]. Fig. 3(h) shows no PL signals in the 800-1600 nm band when using excitation of 1064 nm, which means color centers with emissions in 800-1600 nm band, like $V_{Si}V_C$ and N_CV_{Si}, cannot be prepared by using ion implantation alone, partially because their composite configurations require migration and recombination of simple defects like vacancies.

After annealing treatment, the PL signal of V_{Si} greatly reduced and almost disappeared, meanwhile, two new PL emissions appears in visible and infrared telecom wavelengths. When using excitation wavelength of 1064 nm, a broad peak centered at around 1250 nm appears at room temperature in annealed samples, as shown in Fig. 3(i). The results of low temperature PL measurement at 77 K using InGaAs detector in Fig. 4(b) exhibits two ZPLs at 1178 nm and 1243 nm in the implanted and annealed sample with a dose of 1.3×10^{16} cm^{-2}, corresponding to the PLX4(*kh*) and PLX3(*hk*) c-axis-oriented (axial) configurations of N_CV_{Si} centers in 4H-SiC [17], from which it is evident that N_CV_{Si} centers in 4H-SiC are successfully fabricated by focused He^+ implantation and subsequent annealing treatment. Indeed, the axial N_CV_{Si} centers with C_{3v} symmetry in 4H-SiC has been effectively spin-polarized by the near infrared at around 980 nm, which is advantageous for biological applications [23]. The possible transformation of V_{Si} to N_CV_{Si} in silicon carbide has been approved by density functional theory [41] as well as in experiments [4, 17, 42-44]. Moreover, when using 532 nm excitation, a broad peak center at 700 nm appears at room temperature in annealed samples. However, when we brought the PL measurement temperature down to 77 K, the intensity of the emission decreased but no ZPL is observed. In order to confirm its origin, we employed a 405 nm laser to excited the PL spectrum, the results of which are shown in Figs. S1 and S2 in the supplementary information (SI) and were compared to the spectrum excited by 532 nm. In addition to the green PL emission at 520 nm which might be attributed to the nitrogen/deep-boron donor-acceptor-pair (DAP) transitions [45], the 700 nm emission also appears when using 405 nm excitation. The presence of this 700 nm emission using two different wavelength excitation confirms that it is a PL peak that appears after implantation and annealing, and its luminous position is practically

the same with the phonon-side band of the $C_{Si}V_C$ centers at room temperature [46]. The formation of $C_{Si}V_C$ after thermal annealing at the expense of V_{Si} has already been approved by both experimental studies [1, 46-48] and theoretical calculation [49].

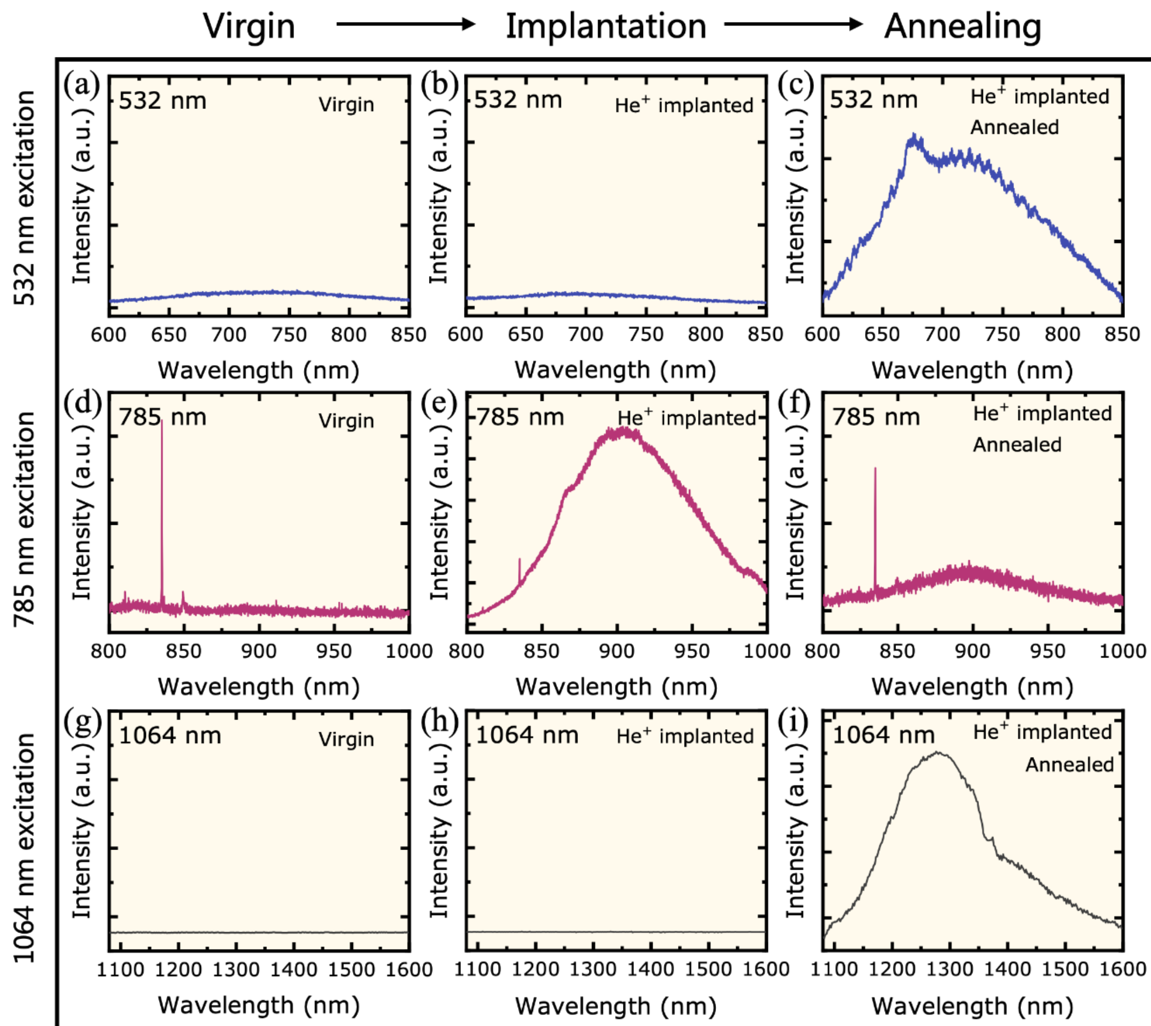

Fig. 3. Room temperature PL spectrum measured at three stages of fabrication: virgin sample (a)(d)(g); He^+ implanted sample without annealing (b)(e)(h); He^+ implanted sample with annealing treatment that heating to 1000 °C at N_2 atmosphere for 1 hour. The spectrum in (b-c) and (e-f) were obtained from samples with implantation dose on the order of 10^{17} cm^{-2} whereas those in (h) and (i) were obtained from the sample with implantation dose of 2.6×10^{15} cm^{-2}.

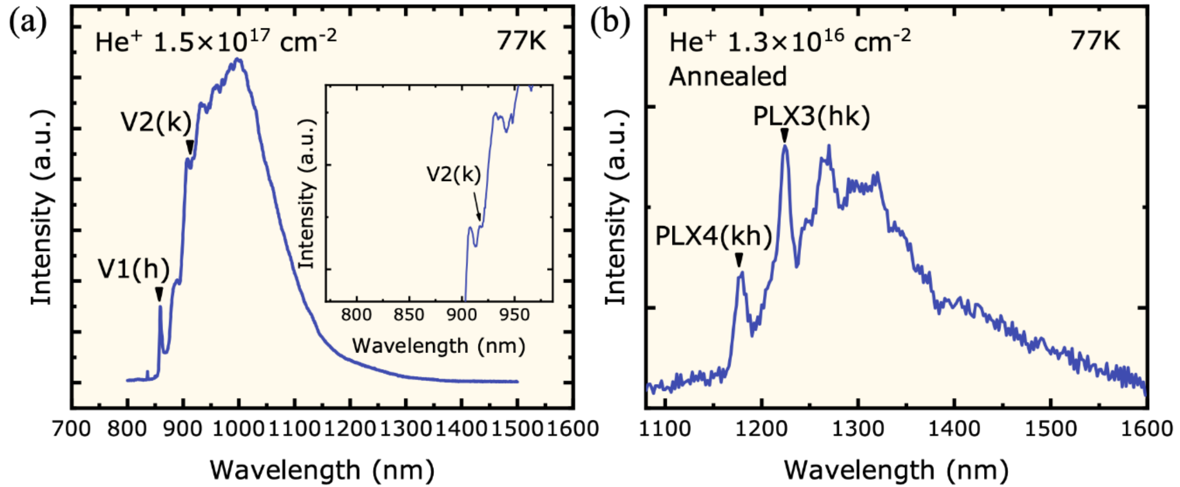

Fig. 4. (a)ZPLs of V_{Si} center (V1 and V2) from PL measurement at 77 K on the sample of 1.5 $\times 10^{17}$ cm^{-2} He^+ implanted 4H-SiC using wavelength of 785 nm excitation and InGaAs detector. (b) ZPLs of N_CV_{Si} center (PLX3 and PLX4) from PL measurement at 77 K on the sample of 1.5 $\times 10^{17}$ cm^{-2} He^+ implanted 4H-SiC using wavelength of 1064 nm excitation and InGaAs detector.

3.4 Distribution of point defects and residual stress analysis

Defect transformation from V_{Si} center to $C_{Si}V_C$ and N_CV_{Si} centers has been observed in the PL spectrum presented above. Furthermore, the distribution of the three types of point defects was investigated by PL mapping and line-scan measurement and the results can be seen from Fig. 5. As reported by our previous results [34], the distribution of V_{Si} after implantation without annealing presents a weak distribution in the middle and strong around for doses above 5×10^{15} cm^{-2}, as shown in Fig. 5(a), which is in agreement with the aforementioned TEM and CL results. N_CV_{Si} centers in SiC, whose optical property is preferable to N_CV_{Si} centers in diamond since its higher efficiency in penetrating biological tissues [50] with near-infrared emission, have not been found in as grown silicon carbide [23]. Hence, generally, both ion implantation and thermal annealing procedures are required to allow the formation of N_CV_{Si} centers in SiC, among which the former is used to introduce predominately vacancies and interstitials, whereas the latter is used to activate the mobility of vacancies and interstitials and to form close pair centers like N_CV_{Si}. It is known from the literatures that silicon vacancies become mobile and are annealed out for temperatures above 750 ℃ [51], and the ZPLs of

N_CV_{Si} in 4H-SiC become noticeable with increased annealing temperatures from 800 to 1050 °C [42].

Thus, we annealed the sample in N_2 atmosphere at 1000 °C for 1 hour to promote the formation of composite pair centers. In visible band, we arranged the intensity of $C_{Si}V_C$ center at the wavelength range from 650 to 800 nm according to the measurement position with sampling step of 0.5 μm in both *x* and *y* direction, as displayed in Fig. 5(b). For high dose implantation of 1.4×10^{17} cm^{-2} and 3.1×10^{17} cm^{-2}, helium bubbles observed in TEM photograph will swell more and burst eventually during thermal annealing, causing rupture to the sample surface, as labeled by *A*, *B*, and *C* in the insert micrograph in Fig. 5(b). The three red dotted circles drawn in the $C_{Si}V_C$ intensity map correspond to the approximate ranges of the three damage locations, *A*, *B*, and *C*, while the black dotted squares illustrate the implanted region of 5×5 μm^2. Interestingly, the strongest emission of $C_{Si}V_C$ center is found near the edge of surface damage regions, which is presumably originated in the relatively thorough stress release and lattice repair at the edge of the damage areas, leading to less luminescence quenching and stronger emission. Next, in near infrared band, we performed spectral measurement to find the optimized dose for the fabrication of N_CV_{Si} centers. It is evident that He^+ implanted region with a dose of 2.6×10^{15} cm^{-2} has the highest intensity of $N_{Si}V_C$ center, as shown in Fig. 9(c). Then, we explored the distribution of N_CV_{Si} centers with different doses using line scan measurement with sampling step of 0.5 μm across the implanted region. Because of the limited collection efficiency of the single point InGaAs detector itself, we use less time-consuming line-scan rather than surface mapping to study the distribution of N_CV_{Si} center, so as to avoid the unexpected interference such as defocusing caused by vibration that may exist during long image-scanning times. The step of line-scan is set as 0.5 μm as well. For doses from 8.2×10^{14} cm^{-2} to 1.3×10^{16} cm^{-2}, the luminescence of the N_CV_{Si} color center is concentrated in the center of the implanted region which is indicated by a pair of gray dash lines. Nevertheless, for dose of 1.4×10^{17} cm^{-2}, the edge of the implanted area has a stronger signal than the center of the implanted area, which is attributed to the material deficiency caused by burst of bubbles during thermal annealing. Moreover, the optimal implantation dose for fabricating N_CV_{Si} center is 2×10^{15} cm^{-2} in the investigated doses here.

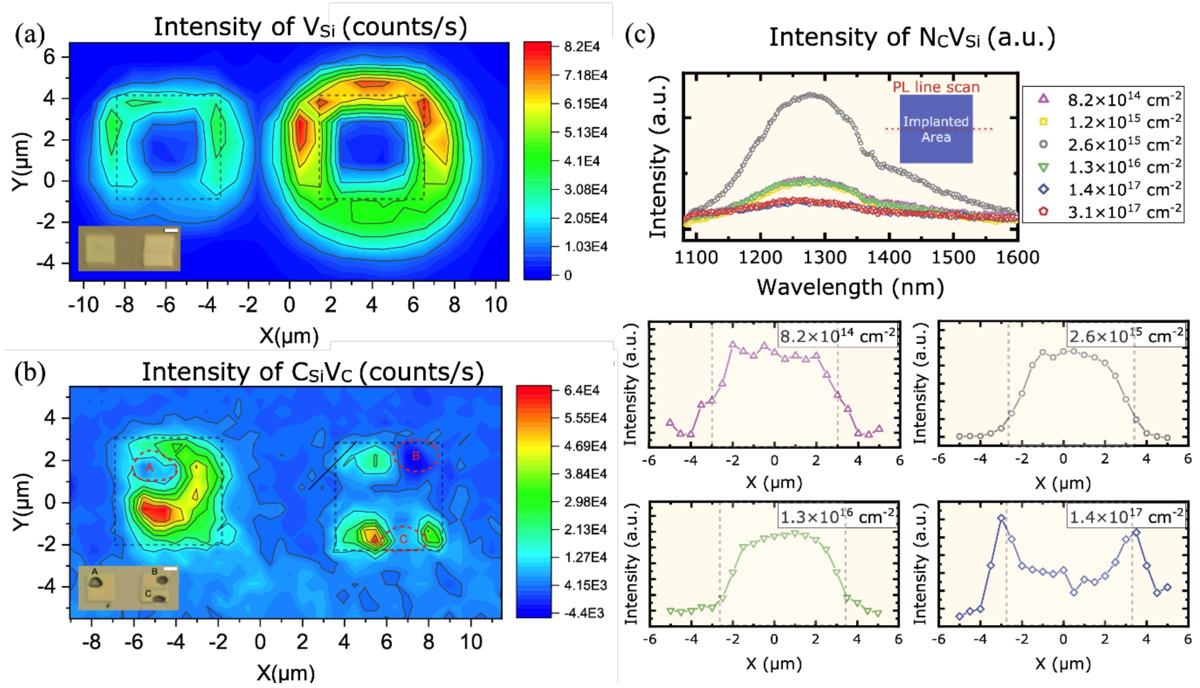

Fig. 5. (a) PL mapping of V_{Si} defects with emission centered at ~900 nm for doses of 1.4×10^{17} cm^{-2} (left) and 3.1×10^{17} cm^{-2} (right) without annealing treatment, respectively. (b) PL mapping of $C_{Si}V_C$ defects with emission at ~700 nm for doses of 1.4×10^{17} cm^{-2} (left) and 3.1×10^{17} cm^{-2} (right) after annealing, respectively. The gray dashed squares in (a) and (b) indicate the implanted regions. (c) PL spectrum and corresponding line-scan results across the implanted area in He^+ implanted and thermal annealed samples using excitation of 1064 nm. The insert diagram in spectrum is the schematic diagram of PL line scan. The pair of gray dash lines in each N_CV_{Si} intensity plot indicate the implanted regions with a distance of 5 μm. The scales in the inset micrographs in (a) and (b) are 2 μm.

In addition to the luminescence distribution of different color centers before and after thermal annealing, the residual stress distribution with different doses is also studied to reveal the possible connection between the defect transformation and the stress release in annealing procedure. Moreover, stress may affect the luminescence properties of color centers, like the ZPL shift in hBN [52], which is also noteworthy in the analysis. As a fast and non-destructive technology, confocal Raman spectroscopy has been widely used in residual stress analysis in SiC materials, such as investigating the velocity effect of grit on cumulative damage in SiC workpiece [53], characterizing the stress of the interface [54], identifying the stress components in SiC power devices [55], and determining irradiation-induced microstructure change in SiC for nuclear applications [56, 57].

Here, we measured the uniaxial stress and select the frequency of E_2 mode ($\Delta\nu$) as the stress indicator in view of its high signal to noise ratio. Confocal Raman measurement was performed using excitation power lower than 1 mW (532 nm) on the sample to refrain from sample modification at the focal point caused by high energy laser irradiation which is prone to occur in implanted regions, and to prevent the disruptive frequency shift of Raman modes caused by thermal expansion [58]. Grating with 1800 grooves per mm was used to ensure enough spectral resolution better than 1 cm^{-1}. Moreover, a mercury lamp was used as the reference spectrum to eliminate the systematic errors, which are caused by Raman spectrometer drifts from the change of instrumental and environmental conditions over long timescales, and thus give an improved wavenumber precision of ±0.05 cm^{-1}[59]. As illustrated in Fig. 6(a), there are two sources in spectral acquisition, including an excitation laser of 532 nm denoted in green color which is used for the excitation of Raman modes, and a mercury lamp denoted in red to give reference for calibration. The scattered Raman signal from the sample together with the reference Hg line from the mercury lamp source were collected to the spectrometer through the inlet slit and detected by the CCD. In each spectrum, Hg line and E_2 Raman modes were collected at the same time, as shown in the spectral diagram in Fig. 6(a) and the spectra in Figs. 6(b-c), where Hg line is shown in red and E_2 Raman mode is shown in blue for clarity. To obtain the credible peak position, the positions of Hg line and E_2 mode were firstly fitted using Gaussian-Lorentz function. Then, the deviation ($\Delta\boldsymbol{\omega}_c$) between the fitted Hg line position the standard Hg line position was calculated as systematic error at the current sampling point, by which the measured E_2 mode position noted as $\boldsymbol{\omega}$ can be corrected according to the formula $\boldsymbol{\omega}_s=\boldsymbol{\omega}-\Delta\boldsymbol{\omega}_c$, where $\boldsymbol{\omega}_s$ is used as the true value of E_2 Raman peak position in subsequent stress analysis. Actually, Hg lines from the mercury lamp cover a wide wavelength range from around 250 to 900 nm and the Hg line of 546.08 nm was chosen as the calibration standard for the measurement, given the proximity of its peak position to E_2 mode. Figs. 6(b) and 6(c) display two spectra from virgin and implanted region, respectively. Since both spectra have been calibrated on the basis of Hg line, the position of the Hg line shows the same location at 546.08 nm, corresponding to a wavenumber of 495.39 cm^{-1} when using 532 nm excitation. Compared with the E_2 mode position of un-implanted area in Fig. 6(b), which is regarded as the stress-free state of the sample, a shift to lower wavenumbers of E_2 mode is observed in implanted region as proved in Fig. 6(c), suggesting tensile stress existed after implantation [60].

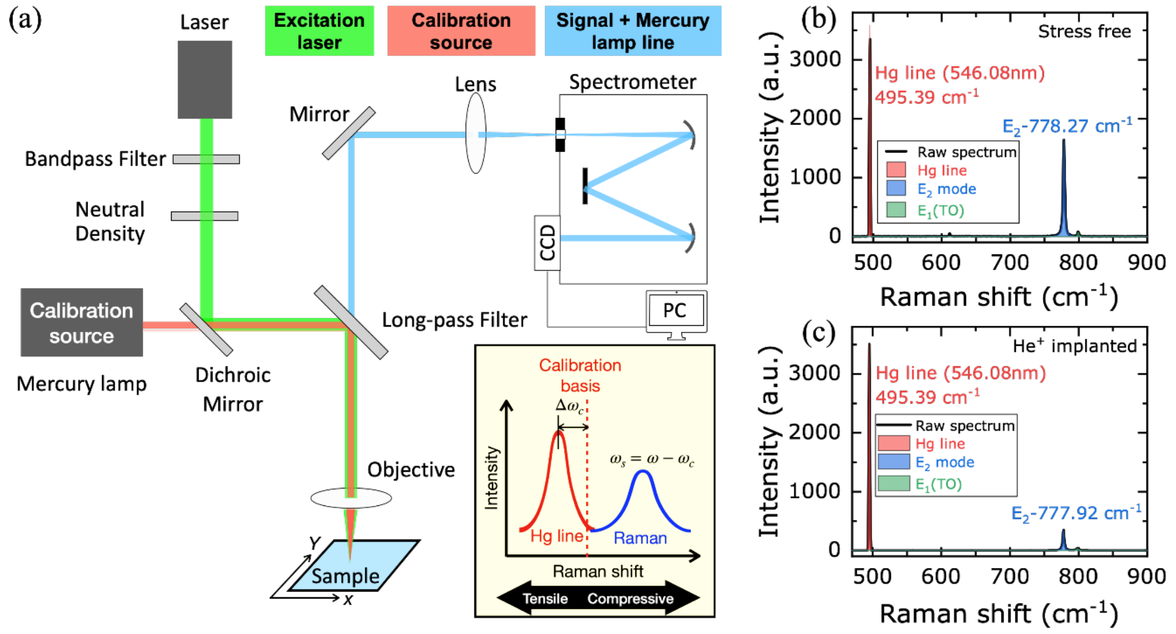

Fig 6. (a) Illustration of experimental setups in Raman stress measurement. (b) Raman spectrum together with a Hg line in un-implanted region. (c) Raman spectrum together with a Hg line in He^+ implanted region with a dose of 1.3×10^{17} cm^{-2}.

Further, we carried out a series of 10 μm ×10 μm Raman surface mapping test with a step of 0.5 μm in both *x* and *y* direction for implanted areas with different doses. In each spectrum, baseline correction was conducted followed by peak fitting of Hg line and E_2 Raman mode by *Labspec 6* software (Horiba Scientific) according to the function of Gauss-Lorentz equation which give the accurate position of Hg line and E_2 mode. Then, the position of E_2 mode in each sampling point was carefully calibrated according to the Hg line of 495.39 cm^{-1} to eliminate systematic error, and the results are given in Figs. 7(a-d) and (i-l), corresponding to the mapping of E_2 Raman mode before and after annealing treatment in implanted regions, respectively. In this study, we adopt the equal biaxial stress assumption, that is: $\Delta\omega_{obs} = \kappa_0\sigma$, where $\Delta\omega_{obs} = \omega - \omega_0$ is the difference between the observed Raman peak position ω and the peak position in the stress-free state ω_0, κ_0 is Raman frequency shift-stress coefficient and we take -321 MPa/cm^{-1} [54] for calculation. To obtain the Raman shift in stress-free state, ω_0, more than 5 points were randomly selected in the un-implanted area over 100 μm away from the implanted area. As a consequence, the peak position of E_2 mode obtained by multi-point measurement is 778.27 ± 0.02 cm^{-1}, and thus 778.27 cm^{-1} is chosen as the reference E_2 mode position of stress-free state. Afterwards, we quantitatively calculated the corresponding stress

distribution in implanted regions according to the formula $\sigma = -321\Delta\omega_{obs}$, as shown in Figs. 7(e-h) and (m-p).

Before annealing treatment, the tensile stress in region implanted with a dose of 2.6×10^{15} cm^{-2} and 1.3×10^{16} cm^{-2} is concentrated in the central part of the implanted area and on the order of 60 MPa and 120 MPa, respectively. In region implanted with dose of 1.3×10^{17} cm^{-2} and 3.2×10^{17} cm^{-2}, the tensile stress increased up to about 160 MPa, and some compressive stress shows up at the boundary between the implanted zone and the un-implanted zone for doses of 1.3×10^{17} cm^{-2} and 3.2×10^{17} cm^{-2}. This corresponds well with the study of Yang et al about the stress in 100 keV He^+ implanted 4H-SiC [60]. After annealing, for doses of 2.6×10^{15} cm^{-2} and 1.3×10^{16} cm^{-2}, no Raman shift can be distinguished in implanted regions, which is a sign that the stress introduced by the low and medium dose implantation has been repaired almost completely. Nevertheless, the E_2 mode shows a frequency shift towards high wavenumbers for doses of 3.2×10^{17} cm^{-2} and 1.3×10^{17} cm^{-2}, indicating the existence of compressive stress, which is also observed and more pronounced in the average hydrostatic stress predicted by MD simulation [61]. The discrepancy between the magnitude of stress is presumably attributed to the difference in sampling volume, which is in scale of μm^3 for experiment and nm^3 for MD simulation. Moreover, the most obvious compressive stress of around -90 MPa is observed at the edge of the area where the helium bubble burst.

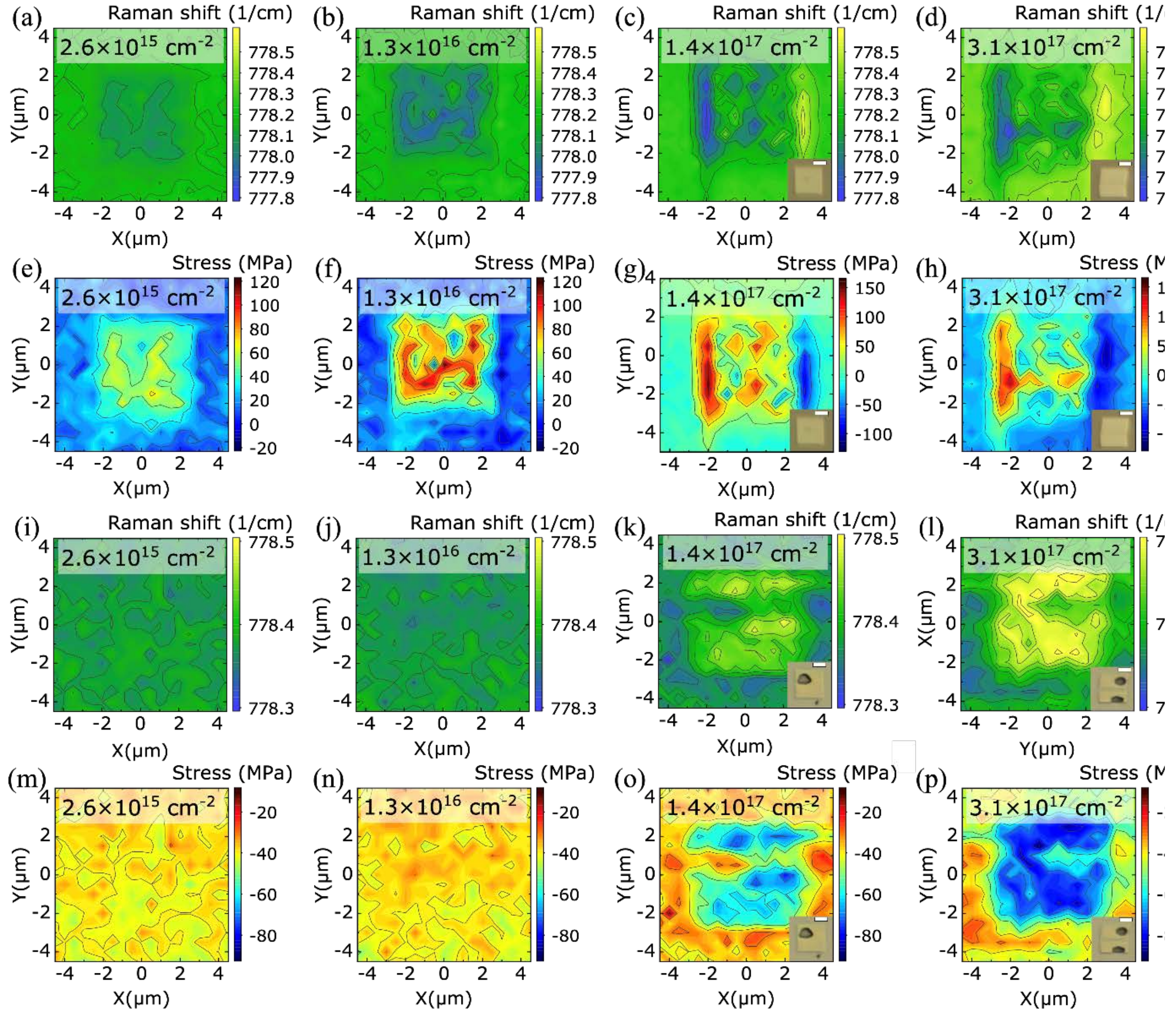

Fig. 7. (a)-(d), (i)-(l) are the mapping results of E_2 Raman mode before and after annealing, with doses range from 2.6×10^{15} to 3.1×10^{17} cm^{-2}, respectively. (e)-(h), (m)-(p) are the calculated stress mappings before and after annealing according to the formula $\sigma = -321\Delta\omega_{obs}$, with doses range from 2.6×10^{15} to 3.1×10^{17} cm^{-2}.

The connection between defect transformation and stress relaxation of the implanted regions is expected, thereby we compare the intensity distribution $C_{Si}V_C$ centers to the stress distribution in implanted regions with a dose of 1.4×10^{17} cm^{-2} after annealing treatment, as displayed in Fig. 8. Overall, the implanted region of 5×5 μm and the damaged position in the left-up corner can be distinguished. It is evident that $C_{Si}V_C$ centers predominantly distributed around the damaged edge where the strongest compressive stress appears which implies the most significant stress repair here.

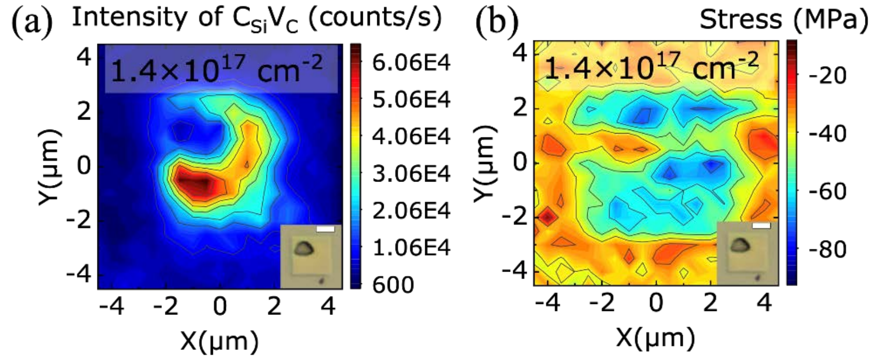

Fig. 8. (a) The intensity of $C_{Si}V_C$ centers in 1.4×10^{17} cm^{-2} He^+ implanted region after annealing. (b) The stress distribution in 1.4×10^{17} cm^{-2} He^+ implanted region after annealing. The scale bar is 2 μm.

Eventually, we summarized the area of N_CV_{Si} and $C_{Si}V_C$ as a function of implantation doses, as plotted in Fig. 9, in which blue circles represent the area of N_CV_{Si} centers and red squares represent the area of $C_{Si}V_C$ centers. N_CV_{Si} area increases with increasing doses, particularly in regions with smaller dwell time of 0.1 μs and 0.5 μs. On the contrary, the $C_{Si}V_C$ area decrease with the increase of doses. This implies a competitive relationship between the formation of $C_{Si}V_C$ and N_CV_{Si} defects. It is generally accepted that N_CV_{Si} and $C_{Si}V_C$ centers arise from the thermal-treatment induced migration and recombination of intrinsic defects and doped impurities like V_{Si}, V_C, C_{Si} and N_C. Therefore, it may be reasonable to suppose that the formation of N_CV_{Si} and $C_{Si}V_C$ both require the consumption of V_{Si} and thus showing a competitive relationship in terms of yield. Our previous study has verified the existence of V_{Si} to $C_{Si}V_C$ conversion during high temperature annealing by MD simulation [49]. And the transformation from V_{Si} to N_CV_{Si} has been systematically studied in [41] by density functional theory. Moreover, for the same dose of around 1×10^{15} cm^{-2}, implantation using smaller dwell time of 0.1 μs yield almost three times of N_CV_{Si} centers than that when using dwell time of 0.5 μs, suggesting that dwell time is another fabrication parameter that needs to be carefully considered and optimized in addition to implantation energy and dose for the generation of N_CV_{Si} centers.

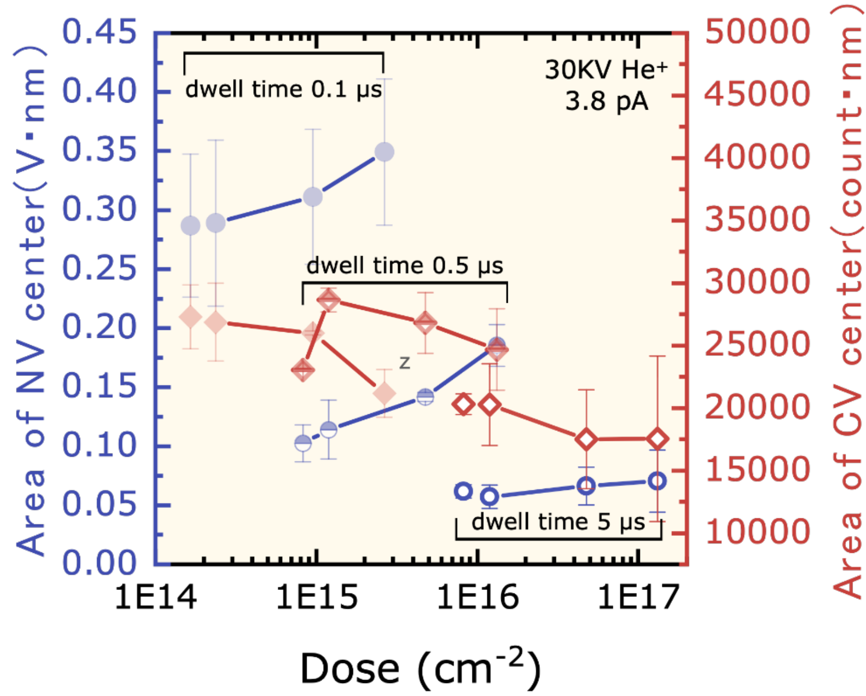

Fig. 9. The area of N_CV_{Si} center and $C_{Si}V_C$ centers as a function of implantation doses. Three groups of data were collected from implanted and annealed regions with different dwell time (0.1 μs, 0.5 μs and 5 μs) during implantation. The area of N_CV_{Si} centers is recorded using the integration of intensity in wavelength range from 1078 to 1600 nm in the unit of *V·nm*, because the output of the intensity is volts for the InGaAs single point detector we used in this study. The area of $C_{Si}V_C$ center is recorded in wavelength range from 600 to 800 nm.

4. Conclusion

We fabricated the V_{Si} color centers by selective He^+ implantation using helium ion microscope (HIM) and observed the transformations from V_{Si} to $C_{Si}V_C$ and N_CV_{Si} defects after thermal annealing at 1000 °C. Cross-sectional TEM revealed the presence of helium bubbles in center of the implanted region with doses of 5.6×10^{16} cm^{-2} and 5.0×10^{17} cm^{-2} which account for the quench of the emission in center of the implanted regions observed in both PL and CL measurements. Based on the comparison between stress distribution and $C_{Si}V_C$ defect distribution, it was evident that $C_{Si}V_C$ centers predominantly distributed around the surface rupture region after thermal annealing where significant stress repair occurred. Moreover, as the increase of the implantation dose, the integral area N_CV_{Si} centers increases whereas the that of $C_{Si}V_C$ decreases, which implies a competitive relationship between the formation of $C_{Si}V_C$ and N_CV_{Si} defects. Apart from that, to fabricate N_CV_{Si} center, who has higher efficiency in penetrating biological tissues due to the preferable wavelengths, a smaller dwell time of 0.1 μs

has been found to be much more efficient in the yield of N_CV_{Si} centers in the investigated dose range.

To conclude, we experimentally demonstrate the generation of V_{Si}, $C_{Si}V_C$, and N_CV_{Si} color centers in 4H-SiC using focused He ion beam with subsequent annealing, and provide insights for the distribution and the competitive relationship among those three kinds of defects. Compared with the ion implantation with an electron beam mask, focused helium ion implantation in this study is more suitable and flexible for its simplified procedure in the precise coupling of emitters to photonic cavity or waveguide which needs integration accuracy in the order of tens of nanometers [5]. Finally, the results of this study provide important support for enriching the preparation of SiC color centers by HIM and the controllable manufacturing of different color centers in SiC.

Acknowledgements

The authors gratefully acknowledge support from National Natural Science Foundation of China (Nos. 52035009, 51761135106), 2020 Mobility Programme of the Sino-German Center for Research Promotion (M-0396), and the ‘111' project by the State Administration Foreign Experts Affairs and the Ministry of Education of China (Grant No.B07014).We thank Dr. Peng Miao, Mr. Xuanshuo Zhang, Ms. Yumei Pu from HORIBA, Dr. Hong Wang from Tianjin Polytechnic University and and Dr. Tao Xue from Tianjin University for help in spectral measurement and valuable discussions. We thank Dr. Jun Xu and Dr. Rui Zhu from Peking University for the helps on HIM implantation.

Reference

[1] S. Castelletto, B.C. Johnson, V. Ivády, N. Stavrias, T. Umeda, A. Gali, T. Ohshima, A silicon carbide room-temperature single-photon source, Nature Materials, 13 (2013) 151-156.

[2] T.C. Hain, F. Fuchs, V.A. Soltamov, P.G. Baranov, G.V. Astakhov, T. Hertel, V. Dyakonov, Excitation and recombination dynamics of vacancy-related spin centers in silicon carbide, Journal of Applied Physics, 115 (2014) 133508.

[3] F. Fuchs, B. Stender, M. Trupke, D. Simin, J. Pflaum, V. Dyakonov, G.V. Astakhov, Engineering near-infrared single-photon emitters with optically active spins in ultrapure silicon carbide, Nature Communications, 6 (2015) 7578.

[4] H.J. von Bardeleben, J.L. Cantin, E. Rauls, U. Gerstmann, Identification and magneto-optical properties of the NV center in 4H-SiC, Physical Review B, 92 (2015) 064104.

[5] J.F. Wang, Y. Zhou, X.M. Zhang, F.C. Liu, Y. Li, K. Li, Z. Liu, G.Z. Wang, W.B. Gao, Efficient Generation of an Array of Single Silicon-Vacancy Defects in Silicon Carbide, Physical Review Applied, 7 (2017) 064021.

[6] J.-F. Wang, J.-M. Cui, F.-F. Yan, Q. Li, Z.-D. Cheng, Z.-H. Liu, Z.-H. Lin, J.-S. Xu, C.-F. Li, G.-C. Guo, Optimization of power broadening in optically detected magnetic resonance of defect spins in silicon carbide, Physical Review B, 101 (2020) 064102.

[7] J.Y. Zhou, Q. Li, Z.Y. Hao, F.F. Yan, M. Yang, J.F. Wang, W.X. Lin, Z.H. Liu, W. Liu, H. Li, L.X. You, J.S. Xu, C.A.F. Li, G.C. Guo, Experimental Determination of the Dipole Orientation of Single Color Centers in Silicon Carbide, ACS Photonics, 8 (2021) 2384-2391.

[8] G. Wolfowicz, S.J. Whiteley, D.D. Awschalom, Electrometry by optical charge conversion of deep defects in 4H-SiC, Proceedings of the National Academy of Sciences of the United States of America, 115 (2018) 7879-7883.

[9] H. Kraus, V.A. Soltamov, F. Fuchs, D. Simin, A. Sperlich, P.G. Baranov, G.V. Astakhov, V. Dyakonov, Magnetic field and temperature sensing with atomic-scale spin defects in silicon carbide, Scientific Reports, 4 (2014) 5303.

[10] D. Simin, V.A. Soltamov, A.V. Poshakinskiy, A.N. Anisimov, R.A. Babunts, D.O. Tolmachev, E.N. Mokhov, M. Trupke, S.A. Tarasenko, A. Sperlich, P.G. Baranov, V. Dyakonov, G.V. Astakhov, All-Optical dc Nanotesla Magnetometry Using Silicon Vacancy Fine Structure in Isotopically Purified Silicon Carbide, Physical Review X, 6 (2016) 031014.

[11] D. Simin, F. Fuchs, H. Kraus, A. Sperlich, P.G. Baranov, G.V. Astakhov, V. Dyakonov, High-Precision Angle-Resolved Magnetometry with Uniaxial Quantum Centers in Silicon Carbide, Physical Review Applied, 4 (2015) 014009.

[12] J.F. Wang, L. Liu, X.D. Liu, Q. Li, J.M. Cui, D.F. Zhou, J.Y. Zhou, Y. Wei, H.A. Xu, W. Xu, W.X. Lin, J.W. Yan, Z.X. He, Z.H. Liu, Z.H. Hao, H.O. Li, W. Liu, J.S. Xu, E. Gregoryanz, C.F. Li, G.C. Guo, Magnetic detection under high pressures using designed silicon vacancy centres in silicon carbide, Nature Materials, 22 (2023) 489-494.

[13] A.L. Falk, P.V. Klimov, B.B. Buckley, V. Ivady, I.A. Abrikosov, G. Calusine, W.F. Koehl, A. Gali, D.D. Awschalom, Electrically and Mechanically Tunable Electron Spins in Silicon Carbide Color Centers, Physical Review Letters, 112 (2014) 187601.

[14] A.N. Anisimov, D. Simin, V.A. Soltamov, S.P. Lebedev, P.G. Baranov, G.V. Astakhov, V. Dyakonov, Optical thermometry based on level anticrossing in silicon carbide, Scientific Reports, 6 (2016) 33301.

[15] Y. Zhou, J.F. Wang, X.M. Zhang, K. Li, J.M. Cai, W.B. Gao, Self-Protected Thermometry with Infrared Photons and Defect Spins in Silicon Carbide, Physical Review Applied, 8 (2017) 044015.

[16] W.F. Koehl, B.B. Buckley, F.J. Heremans, G. Calusine, D.D. Awschalom, Room temperature coherent control of defect spin qubits in silicon carbide, Nature, 479 (2011) 84-88.

[17] S.A. Zargaleh, B. Eble, S. Hameau, J.L. Cantin, L. Legrand, M. Bernard, F. Margaillan, J.S. Lauret, J.F. Roch, H.J. von Bardeleben, E. Rauls, U. Gerstmann, F. Treussart, Evidence for near-infrared photoluminescence of nitrogen vacancy centers in 4H-SiC, Physical Review B, 94 (2016) 060102.

[18] Y.Z. Wu, F. Jelezko, M.B. Plenio, T. Weil, Diamond Quantum Devices in Biology, Angewandte Chemie-International Edition, 55 (2016) 6586-6598.

[19] Y. Ninio, N. Waiskopf, I. Meirzada, Y. Romach, G. Haim, S. Yochelis, U. Banin, N. Bar-Gill, High-Sensitivity, High-Resolution Detection of Reactive Oxygen Species Concentration Using NV Centers, ACS Photonics, 8 (2021) 1917-1921.

[20] E. Janzen, A. Gali, P. Carlsson, A. Gallstrom, B. Magnusson, N.T. Son, The silicon vacancy in SiC, Physica B-Condensed Matter, 404 (2009) 4354-4358.

[21] W.F. Koehl, B. Diler, S.J. Whiteley, A. Bourassa, N.T. Son, E. Janzen, D.D. Awschalom, Resonant optical spectroscopy and coherent control of Cr4+ spin ensembles in SiC and GaN, Physical Review B, 95 (2017) 035207.

[22] J.F. Wang, Q. Li, F.F. Yan, H. Liu, G.P. Guo, W.P. Zhang, X. Zhou, L.P. Guo, Z.H. Lin, J.M. Cui, X.Y. Xu, J.S. Xu, C.F. Li, G.C. Guo, On-Demand Generation of Single Silicon Vacancy Defects in Silicon Carbide, ACS Photonics, 6 (2019) 1736-1743.

[23] H.J. von Bardeleben, J.L. Cantin, A. Csóré, A. Gali, E. Rauls, U. Gerstmann, NV centers in 3C,4H, and 6H silicon carbide: A variable platform for solid-state qubits and nanosensors, Physical Review B, 94 (2016) 121202.

[24] L. Spindlberger, A. Csore, G. Thiering, S. Putz, R. Karhu, J. Ul Hassan, N.T. Son, T. Fromherz, A. Gali, M. Trupke, Optical Properties of Vanadium in 4H Silicon Carbide for Quantum Technology, Physical Review Applied, 12 (2019) 014015.

[25] T. Bosma, G.J.J. Lof, C.M. Gilardoni, O.V. Zwier, F. Hendriks, B. Magnusson, A. Ellison, A. Gallstrom, I.G. Ivanov, N.T. Son, R.W.A. Havenith, C.H. van der Wal, Identification and tunable optical coherent control of transition-metal spins in silicon carbide, npj Quantum Information, 4 (2018) 48.

[26] Z.X. He, Q. Li, X.L. Wen, J.Y. Zhou, W.X. Lin, Z.H. Hao, J.S. Xu, C.F. Li, G.C. Guo, Maskless Generation of Single Silicon Vacancy Arrays in Silicon Carbide by a Focused He+ Ion Beam, ACS Photonics, (2022).

[27] S. Castelletto, A.F.M. Almutairi, K. Kumagai, T. Katkus, Y. Hayasaki, B.C. Johnson, S. Juomos, Photoluminescence in hexagonal silicon carbide by direct femtosecond laser writing, Optics Letters, 43 (2018) 6077-6080.

[28] B.S. Song, S. Yamada, T. Asano, S. Noda, Demonstration of two-dimensional photonic crystals based on silicon carbide, Optics Express, 19 (2011) 11084-11089.

[29] G. Calusine, A. Politi, D.D. Awschalom, Cavity-Enhanced Measurements of Defect Spins in Silicon Carbide, Physical Review Applied, 6 (2016) 014019.

[30] J.F. Ziegler, M.D. Ziegler, J.P. Biersack, SRIM - The stopping and range of ions in matter (2010), Nuclear Instruments & Methods in Physics Research Section B-Beam Interactions with Materials and Atoms, 268 (2010) 1818-1823.

[31] F. Stumpf, A.A. Abu Quba, P. Singer, M. Rumler, N. Cherkashin, S. Schamm-Chardon, R. Cours, M. Rommel, Detailed characterisation of focused ion beam induced lateral damage on silicon carbide samples by electrical scanning probe microscopy and transmission electron microscopy, Journal of Applied Physics, 123 (2018) 125104

[32] C. Tromas, V. Audurier, S. Leclerc, M.F. Beaufort, A. Declemy, J.F. Barbot, Structure and mechanical properties of He-implanted SiC, Nuclear Instruments & Methods in Physics Research Section B-Beam Interactions with Materials and Atoms, 266 (2008) 2776-2779.

[33] G.W. Egeland, J.A. Valdez, S.A. Maloy, K.J. McClellan, K.E. Sickafus, G.M. Bond, Heavy-ion irradiation defect accumulation in ZrN characterized by TEM, GIXRD, nanoindentation, and helium desorption, Journal of Nuclear Materials, 435 (2013) 77-87.

[34] Y. Song, Z. Xu, R. Li, H. Wang, Y. Fan, M. Rommel, J. Liu, G. Astakhov, G. Hlawacek, B. Li, J. Xu, F. Fang, Photoluminescence and Raman Spectroscopy Study on Color Centers of Helium Ion-Implanted 4H–SiC, Nanomanufacturing and Metrology, 3 (2020) 205-217.

[35] C.H. Zhang, S.E. Donnelly, V.M. Vishnyakov, J.H. Evans, T. Shibayama, Y.M. Sun, A study of the formation of nanometer-scale cavities in helium-implanted 4H-SiC, Nuclear Instruments & Methods in Physics Research Section B-Beam Interactions with Materials and Atoms, 218 (2004) 53-60.

[36] C.H. Zhang, S.E. Donnelly, V.M. Vishnyakov, J.H. Evans, Dose dependence of formation of nanoscale cavities in helium-implanted 4H-SiC, Journal of Applied Physics, 94 (2003) 6017-6022.

[37] Y. Song, Z. Xu, M. Rommel, On the interpretation of confocal spectral depth profiling of color center and carrier concentration by photoluminescence and Raman of implanted 4H–SiC, Ceramics International, 49 (2023) 13392-13404.

[38] L. Ottaviani, P. Hidalgo, H. Idrissi, M. Lancin, S. Martinuzzi, B. Pichaud, Structural characterization of 6H-and 4H-SiC polytypes by means of cathodoluminescence and x-ray topography, Journal of Physics-Condensed Matter, 16 (2004) S107-S114.

[39] E. Vuillermet, N. Bercu, F. Etienne, M. Lazar, Cathodoluminescence Characterization of Point Defects Generated through Ion Implantations in 4H-SiC, Coatings, 13 (2023) 992.

[40] J.A. Gerstenhaber, F.C. Barone, C. Marcinkiewicz, J. Li, A.O. Shiloh, M. Sternberg, P.I. Lelkes, G. Feuerstein, Vascular thrombus imaging in vivo via near-infrared fluorescent nanodiamond particles bioengineered with the disintegrin bitistatin (Part II), International Journal of Nanomedicine, 12 (2017) 8471-8482.

[41] A. Csore, H.J. von Bardeleben, J.L. Cantin, A. Gali, Characterization and formation of NV centers in 3C, 4H, and 6H SiC: An ab initio study, Physical Review B, 96 (2017) 085204.

[42] J.F. Wang, F.F. Yan, Q. Li, Z.H. Liu, H. Liu, G.P. Guo, L.P. Guo, X. Zhou, J.M. Cui, J. Wang, Z.Q. Zhou, X.Y. Xu, J.S. Xu, C.F. Li, G.C. Guo, Coherent Control of Nitrogen-Vacancy Center Spins in Silicon Carbide at Room Temperature, Physical Review Letters, 124 (2020) 223601.

[43] S.I. Sato, T. Narahara, S. Onoda, Y. Yamazaki, Y. Hijikata, B.C. Gibson, A. Greentree, T. Ohshima, Near Infrared Photoluminescence of NV Centers in High-Purity Semi-Insulating 4H-SiC Irradiated with Energetic Charged Particles, Materials Science Forum, 1004 (2020) 355-360.

[44] J.F. Wang, Z.H. Liu, F.F. Yan, Q. Li, X.G. Yang, L.P. Guo, X. Zhou, W. Huang, J.S. Xu, C.F. Li, G.C. Guo, Experimental Optical Properties of Single Nitrogen Vacancy Centers in Silicon Carbide at Room Temperature, ACS Photonics, 7 (2020) 1611-1616.

[45] Y. Koshka, M. Mazzola, S. Yingquan, C.U. Pittman, Vanadium doping of 4H SiC from a solid source: Photoluminescence investigation, Journal of Electronic Materials, 30 (2001) 220-223.

[46] B. Lienhard, T. Schroder, S. Mouradian, F. Dolde, T.T. Tran, I. Aharonovich, D. Englund, Bright and photostable single-photon emitter in silicon carbide, Optica, 3 (2016) 768-774.

[47] Y. Chiba, Y. Yamazaki, S.I. Sato, T. Makino, N. Yamada, T. Satoh, Y. Hijikata, T. Ohshima, Enhancement of ODMR Contrasts of Silicon Vacancy in SiC by Thermal Treatment, Materials Science Forum, 1004 (2020) 337-342.

[48] M. Rühl, C. Ott, S. Götzinger, M. Krieger, H.B. Weber, Controlled generation of intrinsic near-infrared color centers in 4H-SiC via proton irradiation and annealing, Applied Physics Letters, 113 (2018) 122102.

[49] Y.X. Fan, Y. Song, Z.W. Xu, B. Dong, J.T. Wu, M. Rommel, K. Zhang, J.L. Zhao, R. Zhu, B.S. Li, Q. Li, F.Z. Fang, Molecular dynamics simulation of color centers in silicon carbide by helium and dual ion implantation and subsequent annealing, Ceramics International, 47 (2021) 24534-24544.

[50] A.M. Smith, M.C. Mancini, S.M. Nie, Second window for in vivo imaging, Nature Nanotechnology, 4 (2009) 710-711.

[51] J. Schneider, K. Maier, Point defects in silicon carbide, Physica B: Condensed Matter, 185 (1993) 199-206.

[52] F. Ren, Y.Y. Wu, Z.W. Xu, Creation and repair of luminescence defects in hexagonal boron nitride by irradiation and annealing for optical neutron detection, Journal of Luminescence, 261 (2023) 119911.

[53] Y.F. Zhang, S.L. Zhu, Y.Y. Zhao, Y.H. Yin, A material point method based investigation on crack classification and transformation induced by grit geometry during

scratching silicon carbide, International Journal of Machine Tools & Manufacture, 177 (2022) 103884.

[54] M. Yoshikawa, Y. Fujita, M. Murakami, Stress Characterization of the Interface Between Thermal Oxide and the 4H-SiC Epitaxial Layer Using Near-Field Optical Raman Microscopy, Applied Spectroscopy, 73 (2019) 1193-1200.

[55] R. Sugie, T. Uchida, Determination of stress components in 4H-SiC power devices via Raman spectroscopy, Journal of Applied Physics, 122 (2017) 195703.

[56] T. Koyanagi, Y. Katoh, M.J. Lance, Raman spectroscopy of neutron irradiated silicon carbide: Correlation among Raman spectra, swelling, and irradiation temperature, Journal of Raman Spectroscopy, 49 (2018) 1686-1692.

[57] H.L. Heinisch, L.R. Greenwood, W.J. Weber, R.E. Williford, Displacement damage in silicon carbide irradiated in fission reactors, Journal of Nuclear Materials, 327 (2004) 175-181.

[58] N. Hunter, M. Rahbar, R. Wang, M. Mahjouri-Samani, X. Wang, Determination of a Raman shift laser power coefficient based on cross correlation, Optics Letters, 47 (2022) 6357-6360.

[59] R.S. Jakubek, M.D. Fries, Calibration of Raman wavenumber in large Raman images using a mercury-argon lamp, Journal of Raman Spectroscopy, 51 (2020) 1172-1185.

[60] S.B. Yang, S. Tokunaga, M. Kondo, Y. Nakagawa, T. Shibayama, Non-destructive evaluation of the strain distribution in selected-area He+ ion irradiated 4H-SiC, Applied Surface Science, 500 (2020) 144051.

[61] Y. Fan, Y. Song, Z. Xu, J. Wu, R. Zhu, Q. Li, F. Fang, Numerical study of silicon vacancy color centers in silicon carbide by helium ion implantation and subsequent annealing, Nanotechnology, 33 (2021) 125701.